Available online at www.sciencedirect.com
ScienceDirect
Applied Catalysis B: Environmental 69 (2006) 115–125
APPLIED CATALYSIS B: ENVIRONMENTAL
www.elsevier.com/locate/apcatb

Improved Pd-on-Au bimetallic nanoparticle catalysts for aqueous-phase trichloroethene hydrodechlorination

Michael O. Nutt [a], Kimberly N. Heck [a], Pedro Alvarez [b,c], Michael S. Wong [a,c,d,*]

[a] Department of Chemical and Biomolecular Engineering, Rice University, 6100 Main Street, Houston, TX 77005-1892, USA
[b] Department of Civil and Environmental Engineering, Rice University, 6100 Main Street, Houston, TX 77005-1892, USA
[c] Center of Biological and Environmental Nanotechnology, Rice University, 6100 Main Street, Houston, TX 77005-1892, USA
[d] Department of Chemistry, Rice University, 6100 Main Street, Houston, TX 77005-1892, USA

Received 14 February 2006; received in revised form 26 May 2006; accepted 2 June 2006
Available online 17 July 2006

Abstract

Groundwater remediation through the catalytic breakdown of the undesired contaminants is a more effective and desirable approach than the conventional physical displacement methods of air-stripping and carbon adsorption. Palladium-on-gold nanoparticles (Pd/Au NPs) have recently been shown to catalyze the hydrodechlorination of trichloroethene in water, at room temperature, and in the presence of hydrogen, with the most active Pd/Au material found to be >70 times more active than Pd supported on alumina on a per-Pd atom basis. The potential of this catalyst as a groundwater remediation technology could be improved by synthesizing Pd/Au NPs with smaller diameters and immobilizing them on a solid support. For this study, we synthesized Pd/Au NPs with a core diameter of 4 nm and with different Pd loadings and studied them in colloidal form for aqueous-phase trichloroethene hydrodechlorination. The most active catalysts were considerably more active (>1900 L/g_{Pd}/min) than Pd NPs (55 L/g_{Pd}/min) and conventionally synthesized Pd/Al_2O_3 (47 L/g_{Pd}/min). Accounting for a gas–liquid mass transfer effect and converting the Pd loading to Pd surface coverage using a magic cluster model for the Pd/Au NPs, the reaction rates in terms of initial turnover frequencies were >1.4, 4.35×10^{-2}, and 3.76×10^{-2} s^{-1}, respectively. These materials exhibited volcano-like catalytic activity, in which hydrodechlorination rate was maximum near 70% Pd surface coverage. Au appeared to promote catalysis through geometric and electronic effects. Immobilization of the NPs on alumina, magnesia, and silica supports yielded active oxide-supported catalysts.

Keywords: Palladium; Gold; Nanoparticles; Groundwater; Trichloroethene; Remediation

1. Introduction

Trichloroethene (TCE) is considered one of the most common hazardous organic contaminants found in groundwater [1–5]. Its use as a solvent to degrease metals and electronic parts in the automotive, metals, and electronic industries, with smaller-scale use in chemicals production, textile cleaning, and consumer products has led to its prevalence in our environment, particularly in groundwater. TCE has been linked to liver damage, impaired pregnancies, and cancer in humans [6,7]. Furthermore, natural environmental degradation of TCE can lead to vinyl chloride, which is a more most hazardous organic compound [4,8].

Recently, alternatives to conventional TCE contaminated groundwater treatment methods of air-stripping and carbon adsorption have been investigated, such as bioremediation, reactive remediation, phytoremediation, and in situ thermal treatments [3,9–11]. These methods attempt to convert TCE into a more benign chemical rather than move the contaminant from one phase (water) to another (air/solid), which still requires further treatment. Of these methods, one of the most promising involves the reactive remediation using zero-valent iron nanoparticles as a reagent shown by Zhang and co-workers [12,13].

There is also promise in the development of catalytic remediation technologies that utilize supported palladium metal as a catalysts for chemical reduction [14,15]. Zhang and co-workers illustrated enhanced dehalogenation rate constants when Pd/Fe synthesized metal nanoparticles were used, 30 times greater than iron nanoparticles alone [16–19]. Whereas the iron is the reducing agent in this case, palladium metal can

* Corresponding author. Tel.: +1 713 348 3511; fax: +1 713 348 5478.
E-mail address: mswong@rice.edu (M.S. Wong).

0926-3373/$ – see front matter © 2006 Elsevier B.V. All rights reserved.
doi:10.1016/j.apcatb.2006.06.005

also catalyze the reaction using hydrogen gas as the reducing agent. Reinhard and co-workers focused on the use of commercially available 1 wt% Pd/Al_2O_3 catalysts tested in both laboratory and pilot-scale units while examining the effects of hydrogen concentration, pH, and poisoning/regeneration on TCE and other chlorinated organic dechlorination reactions [20–26]. As an advantage over other remediation approaches, palladium converts TCE into ethane with minimal formation of vinyl chloride and other chlorinated intermediates [21,23] that often occur with anaerobic bioremediation [10] and with iron metal [12].

In our previous work, we compared the TCE HDC catalytic activity of unsupported Pd NPs, Pd supported on alumina (Pd/Al_2O_3), and Pd black, and found that the Pd NPs were more active due to more efficient use of the metal, i.e., higher Pd dispersion [27]. Working towards the goal of increasing the dispersion and reducing the catalyst cost, we discovered that Pd catalytic activity was increased by as much as ~70 times (943 L/g_{Pd}/min) compared to Pd/Al_2O_3 (12 L/g_{Pd}/min), by supporting Pd metal on the surface of Au NPs. This report described the use of a Pd-on-Au (Pd/Au) bimetallic composition for the aqueous-phase remediation of chlorinated compounds for the first time, complementing the work by others on the gas-phase hydrodehalogenation of halogenated compounds [28–30]. The promotion effect of Au on Pd catalytic activity is a well-known phenomenon for a number of model reactions [31–34], including the commercial production of vinyl acetate [35–39]. The general explanations for the synergistic combination of two metals are a geometric effect, an electronic effect, or a combination of both [40], depending on the metal composition and the reaction. The presence of mixed metal active sites and, unique to Pd-based catalysts, the suppression of a less active β-PdH phase have been hypothesized [41,42]. It is not yet known how Au promotes Pd activity for aqueous-phase TCE HDC.

We were motivated by cost reduction considerations to synthesize Pd/Au NPs with smaller diameters than the ~20-nm particles used in our original study. Here, we report the successful synthesis and catalytic properties of Pd/Au NPs with Au particle diameters of 4 nm and with variable Pd loadings. We show that the colloidal NPs exhibit a clear volcano-shape activity dependence on Pd metal content. We identify three regions of catalytic activity and discuss the possible promotion effects of Au on Pd catalysis. Towards a practical catalyst for flow reactor studies and future spectroscopic studies, we present results for a NP immobilization strategy based on electrostatic interactions between the Pd/Au NPs and the porous support.

2. Experimental

2.1. Monometallic NPs

Gold nanoparticles (Au NPs) were synthesized by modifying the method reported by Slot and Geuze [43]. A gold salt solution was prepared by diluting 100 μL of a $HAuCl_4$ solution (0.296 M; $AuCl_3$ 99.99%, Sigma–Aldrich) in 80 mL of Nanopure water (>18 MΩ-cm, Barnstead NANOpure Diamond). A second solution containing 0.04 g trisodium citrate (>99.5%, Fisher), 0.05 g tannic acid (>99.5%, Sigma–Aldrich), and 0.018 g potassium carbonate (>99.5%, Sigma–Aldrich) dissolved in 20 mL of Nanopure water was prepared. Both solutions were stirred while being heated to 60 °C. Once this temperature was reached, the tannic acid solution was added to the gold chloride solution; an immediate color change (from pale yellow to reddish-brown) was observed. The solution was then heated and left to boil for 2 min, and then removed from the heat source. The final fluid had a dark brown-red color. Twenty-nanometer Au NPs (1.16×10^{12} NP/mL) were prepared through the citrate reduction method, as previously described [27].

Palladium nanoparticles (Pd NPs) were synthesized using the-above method by substituting the Au salt solution with a $PdCl_4^{2-}$ solution. A palladium salt solution was prepared by diluting 12 mL of a H_2PdCl_4 solution (2.47 mM; $PdCl_2$, 99.99%, Sigma–Aldrich) in 68 mL of Nanopure water. A second solution containing 0.04 g trisodium citrate (>99.5%, Fisher), 0.05 g tannic acid (>99.5%, Sigma–Aldrich), and 0.018 g potassium carbonate (>99.5%, Sigma–Aldrich) dissolved in 20 mL of Nanopure water was prepared. The procedure was carried in the same manner except that the reaction mixture was boiled for 25 min instead of 2 min. A portion of the water volume (72%) evaporated during the boiling step. The resulting yellow fluid was aged overnight at room temperature, resulting in a coffee-black colored fluid. The NPs were ~4-nm in diameter, according to transmission electron microscopy. 1 wt% Pd/Al_2O_3 (Sigma–Aldrich) was run as a reference sample.

2.2. Pd/Au bimetallic NPs

The synthesis of bimetallic Pd/Au NPs was carried out by mixing specific volume (0–287 μL) of $PdCl_4^{2-}$ solution (2.47 mM) to 2 mL of the Au NP sol (1.26×10^{14} NP/mL) and stirring for at least 15 min. Hydrogen gas (99.99%; Matheson) was then bubbled through the synthesis fluid for 1 min. The resultant NP sol was left to sit at room temperature overnight. A control sample was prepared by bubbling H_2 gas through the Au NP sol without the Pd salt.

2.3. Oxide-supported Pd/Au bimetallic NPs

Three different oxide materials were used as supports for immobilizing the Pd/Au NPs: γ-alumina (Al_2O_3, 99.9%; Strem), magnesium oxide (MgO, 99.9%; Sigma–Aldrich), and silicon oxide (SiO_2, 99.9%; Cabosil–Cabot). For both Al_2O_3 and MgO, 0.47 g of powder were combined with 8 mL of a Pd/Au NP sol and stirred overnight at room temperature. For SiO_2, 0.20 g were suspended in 2.04 mL of ethanol for 10 min. 0.13 g of 3-aminopropyltriethoxysilane (APTES) was then added and stirred overnight. This slurry was washed 3 times with 3.8 mL of ethanol per wash to remove any unbound APTES. This amine-functionalized SiO_2 was combined with 8 mL of a Pd/Au NP sol and stirred overnight at room temperature. The NP-

supported slurry was concentrated through centrifugation and decantation of the supernatant. The supernatant was examined for unbound Pd/Au NPs using UV–vis spectroscopy, which confirmed complete uptake of the catalyst NPs.

Additional immobilization stability tests were conducted using Au NPs instead of Pd/Au NPs. These Au NP-supported materials underwent a washing procedure after contact with the NPs. Nanopure water (6 mL) was added to the powders and stirred for 30 min. The suspensions were centrifuged, and the supernatant removed and analyzed for any Au NPs leached.

2.4. Characterization methods

UV–vis absorbance spectra of the monometallic and bimetallic NP suspensions were collected on a Shimadzu UV-2401 PC spectrophotometer using a quartz cuvette with a 1-cm path length. Au NP surface charge was characterized using Brookhaven Instruments Corporation ZetaPALS dynamic light scattering (DLS) apparatus utilizing a 660-nm wavelength laser and a dip-in (Uzgiris-type) electrode. X-ray diffraction (XRD) patterns of dried NPs and supported catalysts were collected on a Rigaku Ultima D/Max 2100 diffractometer utilizing Cu Kα radiation (λ = 1.5406 Å). Dried NPs were prepared by concentrating 5 mL of the sol to ∼0.5 mL via evaporative drying at 70 °C, depositing the suspension on a glass slide, and drying at 70 °C. Grain size analysis was carried on the (1 1 1) reflection of bulk Pd and Au using Scherrer's formula using Jade MDI software. BET (Brunauer–Emmett–Teller) surface areas and pore volumes of the supported catalyst powders were determined using a Micromeritics ASAP 2010 nitrogen gas adsorption analyzer. The NP materials were imaged using a JEOL 2010 transmission electron microscope (TEM) using 200 kV accelerating voltage and a 0.3 nm resolution. Samples were prepared by depositing 50 μL of solution on a 200-mesh carbon/formvar TEM grid and dried at 70 °C. Particle size distribution measurements were made using the *ImageJ* program [44]. X-ray photoelectron spectra (XPS) of Pd/Au NPs of controlled Pd content (ranging from 10.9 wt% to 48.4 wt%) were collected on a PHI Quantera SXM X-ray photoelectron spectrometer operated at 25.63 W using monochromatized Al Kα radiation (1486.6 eV) with a beam diameter of 100 μm. The XPS samples were prepared by depositing 50 μL of a NP suspension on poly(lysine) coated slides, drying at 50 °C, and rinsing with Nanopure water to remove residual salts like KCl; electrostatic interaction between the negatively charged NPs and the positively charged poly(lysine) secured the NPs on the slide. This deposition/dry/rinse procedure was repeated 40 times for each Pd/Au NP sample. The samples were analyzed in an ultrahigh vacuum (UHV) chamber at 10^{-9} Torr. The core level binding energy for adventitious carbon (C 1s, 284.4 eV) was used as the internal standard [45].

2.5. Catalytic testing

TCE HDC batch reactor experiments were conducted in a manner similar to our previous study, except that larger reaction volumes were used here. Nanopure water (172 mL) and a magnetic stir bar were sealed in Boston Round screw-cap bottle (250 mL, Alltech) with Teflon tape wrapped threads and bubbled with H_2 gas for 15 min to displace dissolved oxygen and to fill the headspace with a hydrogen atmosphere (1 atm). After the bottle was sealed with a teflon-rubber septum and bubbled, ∼7 μL of TCE (99.5%, Aldrich) was added, and 0.2 μL of pentane (99.7%, Burdick and Jackson) was added as an internal standard. The Pd/Au NPs were injected through the septum, such that a total of 6.4×10^{-8} mol of Pd were added. With the total Pd amount being constant, the Pd/Au NP concentrations ranged from 2.1×10^{13}–2.5×10^{14} NP/mL. Sols of Au NPs (1 mL) and Pd NPs (1 mL) were injected into the reactor in control experiments, at particle concentrations of 1.26×10^{14} and 4.5×10^{14} NP/mL, respectively. In testing the catalytic activity of supported Pd/Au NPs, the slurries were diluted in 1.25 mL of water for easier handling before being injected into the reactor. The catalyst weights and metal loadings (based on metal precursor amount) were as follows: twenty milligrams of MgO material (0.015 wt% Pd, 0.10 wt% Au), and 17.4 mg of SiO_2 material (0.040 wt% Pd, 0.23 wt% Au). The catalytic reactions were conducted at room temperature under vigorous magnetic stirring.

The reaction was monitored through headspace gas chromatography (GC), in which 100 μL of headspace gas in the reactor is withdrawn with a gas-tight syringe and injected into an Agilent Technologies 6890 GC equipped with a flame ionization detector (FID) and a packed column (6-in. × 1/8-in. outer diameter) containing 60/80 Carbopack B/1% SP-1000 (Supelco). Calibration curves were prepared for chlorinated ethenes, chlorinated ethanes, and ethane. The initial TCE concentration in the liquid was approximately 60–70 ppm (1 ppm = 1 mg L^{-1}), far below the saturation concentration of 1200 ppm at 25 °C [46].

Reaction rate constants were determined by assuming a first-order rate dependence for the conversion of TCE during HDC [23]:

$$\frac{-\mathrm{d}C_{\mathrm{TCE}}}{\mathrm{d}t} = k_{\mathrm{meas}} C_{\mathrm{TCE}} \quad (1)$$

where the measured, apparent first-order rate constant $k_{\mathrm{meas}} = k_{\mathrm{cat}} \times C_{\mathrm{cat}}$, where k_{cat} is the Pd-normalized reaction rate constant (with units of $L/g_{Pd}/min$), C_{cat} is the concentration of Pd charged to the reaction volume, and C_{TCE} is the TCE concentration in the bulk fluid.

3. Results and discussion

3.1. Synthesis and characterization of Pd/Au NPs using 4-nm Au NPs

To generate Au NPs smaller than the ∼20-nm NPs in our original study [27], we replaced the sodium citrate salt with a tannic acid/sodium citrate solution and reduced the heating time and temperature. This modified synthesis method led to the consistent formation of uniformly sized 4-nm Au NPs (Fig. 1a). The NPs had a Gaussian-like size distribution with a relative standard deviation of 21% (Fig. 1b). The XRD pattern

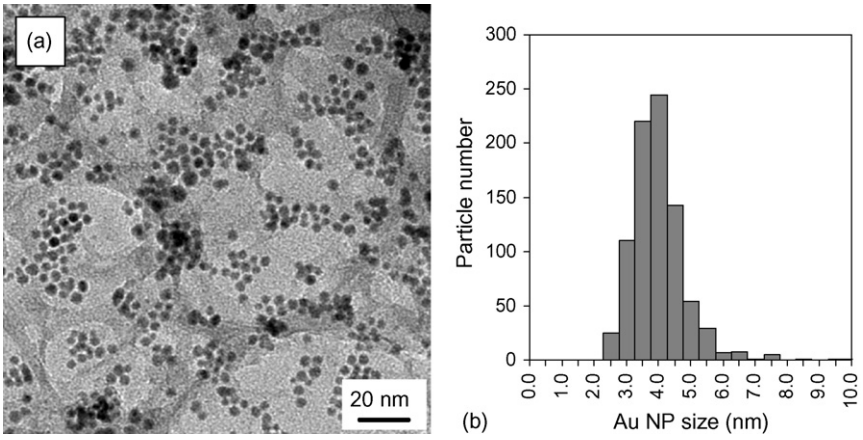

Fig. 1. (a) TEM image and (b) particle size distribution of Au NPs measured from 850 particles in TEM images. Each bar in the histogram represents the total number of NPs counted with diameters ±0.25 nm of average bin size, e.g., 25 NPs with diameters in the 2.25–2.75 nm range was counted.

of these Au NPs presented barely discernible metal diffraction peaks (Fig. 2a and inset). Peak broadening analysis on the (1 1 1) peak of Au ($2\theta = 38.2^\circ$) indicated a grain size of 3.6 nm, indicating that at least a fraction of the NPs were single crystals of Au. The XRD pattern of Au NPs with a TEM particle size of 20 nm and a grain size of 17 nm is shown for comparison (Fig. 2b).

The brown-reddish 4-nm Au NP sol exhibited a weak shoulder near 560 nm in its UV–vis absorbance spectrum (Fig. 3a). For comparison, a suspension of 20-nm Au NPs prepared through citrate reduction was ruby-red in color with the characteristic surface plasmon resonance (SPR) peak at 520 nm (Fig. 3c). A broader, less-intense SPR peak located at the same wavelength was expected for the 4-nm Au NPs [47], but it was obscured significantly by the tannic acid (Fig. 3b).

We prepared a series of Pd/Au NP catalysts with varying Pd weight loadings up to 45 wt% Pd by chemically reducing Pd salt in the presence of Au NPs; dihydrogen gas is a known reducing agent for Pd and other metal salts [48–51]. Generally, the activation energy for heterogeneous nucleation is less than that for homogeneous nucleation [52], particularly if the depositing material completely wets the particle surface, which results in Pd(0) atoms depositing on Au NP surfaces rather than forming Pd NPs. This ‘‘seeded’’ synthesis method represents a type of electroless metal deposition [53] and it has been studied very extensively in the preparation of metal-coated Au NPs and larger Au NPs from smaller Au NP ‘‘seeds’’ [54–59]. This approach is conceptually similar to the synthesis of other core/shell NPs, like CdS-coated CdSe quantum dots [60–62]. It could be possible that Au NPs mediate Pd ion reduction at the particle surface and the deposited Pd metal reduces additional Pd ions autocatalytically, which would lead to Pd coatings instead of discrete Pd NPs. This possibility draws upon recent

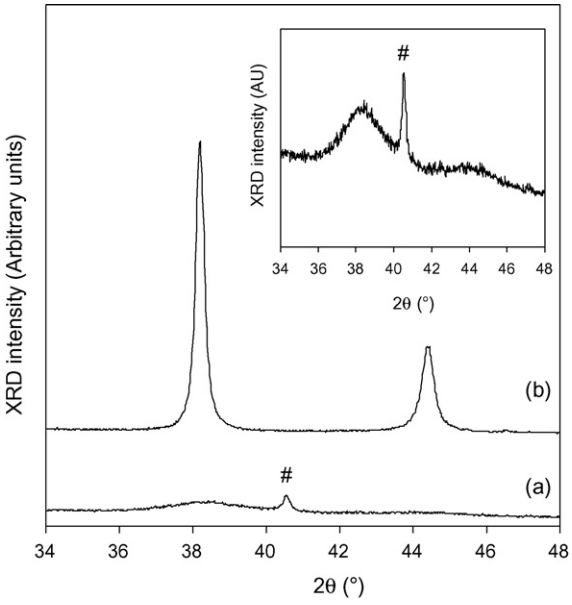

Fig. 2. XRD patterns of dried (a) 4-nm Au NPs from tannic acid/citrate reduction method and (b) 20-nm Au NPs from citrate reduction method. The XRD peak (#) at $2\theta = 40.5^\circ$ comes from residual KCl from the K_2CO_3 and gold chloride precursors used. Inset: re-scaled XRD pattern of 4-nm Au NPs.

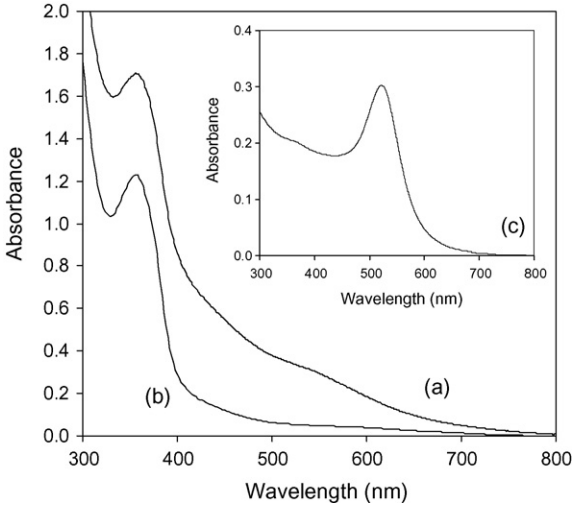

Fig. 3. UV–vis spectra of (a) 4-nm Au NP sols synthesized from tannic acid/citrate reduction, (b) a solution resulting from the tannic acid/citrate reduction method in the absence of the gold precursor. Both liquids were diluted to ~18% of original concentration for UV–vis measurements, and (c) UV–vis spectra of a 20-nm Au NP sol synthesized from citrate reduction method.

Table 1
Magic cluster calculations of Au NPs

Shell number (n)	Number of atoms in shell (n_{atom})[a]	Total number of Au in NP(n_{tot})[b]	Calculated Au NP diameter (nm)
	1	1	0.27
1	12	13	0.80
2	42	55	1.34
3	92	147	1.88
4	162	309	2.41
5	252	561	2.95
6	362	923	3.48
7	492	1415	4.02
8	642	–	–
9	812	–	–

[a] Equation: $n_{atom} = 10n^2 + 2$.
[b] Equation: $n_{tot} = (10n^3 + 15n^2 + 11n + 3)/3$.

observations that nanosized Au activates dihydrogen and catalyzes some hydrogenation reactions [63–65]. There is no galvanic reaction between the surface Au(0) atoms and Pd(II) ions that would complicate the Pd deposition process, as Au has a higher redox potential than Pd [27].

To relate the Pd loading to a core/shell bimetallic structure, we modeled Pd/Au NPs as gold "magic clusters" with a Pd shell of variable coverage. In the magic cluster model [66–68], a NP is treated as a central atom surrounded by closed shells of identical atoms, providing a helpful calculation method for estimating the Au NP concentration and the Pd surface coverage. Four-nanometer Au NPs were approximated as containing seven shells of Au atoms (Table 1); based on the assumption of complete reduction of the Au precursor to form Au NPs, a concentration of 1.26×10^{14} NP/mL was estimated. Pd has an atomic radius of 1.40 Å, close in size to an Au atom (1.35 Å) [69], and so the reductive deposition of Pd atoms onto the Au NP surface was considered to be equivalent to the formation of an eighth shell of metal atoms (Fig. 4). Thus, a 4-nm Au NP with a complete shell of Pd atoms, or 100% Pd coverage, is readily calculated to have a Pd content of 19.7 wt%. Surface coverages above 100% refer to the formation of additional shells on top of the complete eighth Pd shell (Table 2).

We analyzed the Pd/Au NP catalysts through UV–vis spectroscopy, XPS, XRD, and TEM. In the case of the larger Pd/Au NPs studied earlier, the SPR peak absorbance decreased in intensity with increasing amounts of Pd, which indicated the formation of the Pd coating on the Au NPs [27]. Little difference in the UV–vis spectra could be observed for the 4-nm Au NPs with different Pd loadings, though, due to the weak SPR peak of Au. On the other hand, subtle differences were found through XPS measurements. Pd NPs exhibited two photoemission peaks at binding energies of 335.3 and 340.7 eV, which can be assigned, respectively, to Pd $3d_{5/2}$ and Pd $3d_{3/2}$

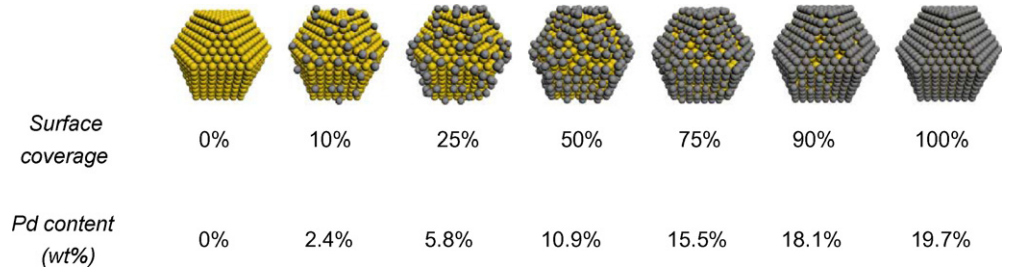

Fig. 4. Schematic of Pd/Au NPs idealized as magic clusters, with a 4-nm Au core and variable Pd surface coverage from 0 to 100% (with corresponding Pd content). The actual Pd/Au NPs will deviate from the model in terms of particle size distribution and spatial distribution of Pd atoms.

Table 2
Pd/Au NP catalyst compositions and rate constants

Pd loading (wt%)	Pd surface coverage (%)	Rate constant k_{cat} (L/g_{Pd}/min)	Mass-transfer-correctedrate constant k_{corr} (L/g_{Pd}/min)	Initial turnover frequency TOF (mol-TCE/mol-Pd/s)
0	0	0	0	0
2.8	11.8	498	518	0.32
5.5	23.8	819	873	0.68
8	35.6	1345	1499	0.80
12.7	59.3	1956	2297	1.43
14.9	71.2	1903	2224	1.47
17.9	89.0	1839	2138	1.18
22	111.8	817	871	0.57 (0.64)[b]
26	134.1	724	766	0.50 (0.66)[b]
41.1	236.5	419	433	0.34 (0.71)[b]
100[a]	–	55	55	0.044 (0.13)[b]
100[c]	–	47	47	0.038

[a] Pure Pd NPs.
[b] Values in parentheses are based on calculated amount of exposed Pd atoms (mol-TCE/mol-surface-Pd/s).
[c] Pd/Al_2O_3, with 1 wt% Pd on total catalyst weight basis and 100 wt% on total metals weight basis.

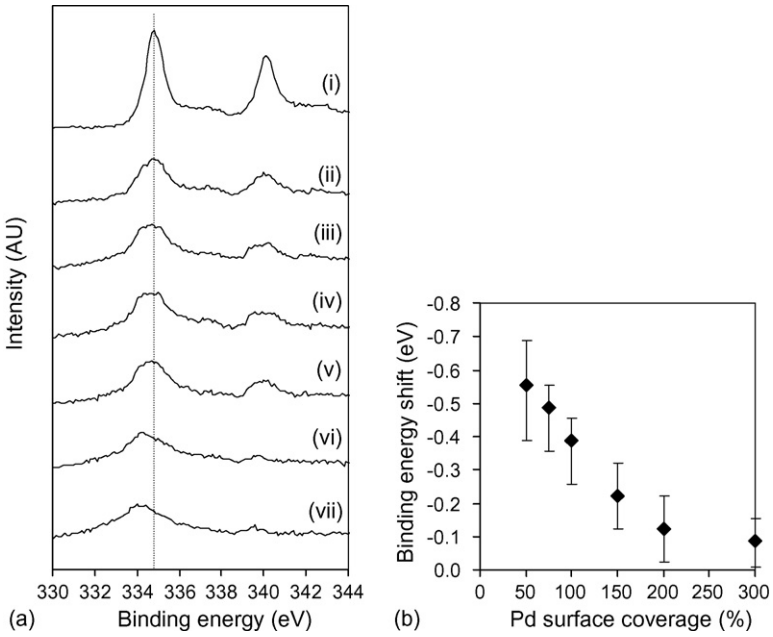

Fig. 5. (a) X-ray photoelectron spectra in the Pd 3d region for (i) Pd NPs and Pd/Au NPs with Pd surface coverages of (ii) 300%, (iii) 200%, (iv) 150%, (v) 100%, (vi) 75%, and (vii) 50% and (b) binding energy shifts from 335.3 eV for Pd/Au NPs as a function of Pd surface coverage.

spin-orbit states of zero-valent Pd (Fig. 5a) [70–72]. The very small shoulder at ~337.3 eV can be assigned to the Pd $3d_{5/2}$ of Pd(II) resulting from the oxidation of metallic Pd during XPS sample preparation [68,71,73]. Focusing on the Pd $3d_{5/2}$ peak, there was a small binding energy shift for Pd/Au samples with Pd surface coverages in excess of 100% (i.e., with multiple Pd layers). With decreasing Pd surface coverage below 100%, the Pd $3d_{5/2}$ peak shifted to lower binding energies, with the energy difference becoming more pronounced (Fig. 5b). These XPS data indicated that the electronic structure of the Pd metal was modified by the Au, which would result only if the Pd metal were in intimate contact with the Au NPs. XRD analysis did not indicate the presence of Pd domains in the Pd/Au NP samples. We performed TEM on Pd/Au NP samples, but we were unsuccessful in imaging the Pd coating on the Au NPs.

3.2. Effect of Pd content on TCE reaction rate

The TCE HDC reaction rate varied significantly with Pd content. Evidenced in the conversion-time profiles, the reaction rate increased significantly from 0 wt% Pd (pure Au NPs) to 12.7 wt%, and decreased with higher Pd content (Fig. 6a and b). The reaction rate constant k_{cat}, derived from the observed first-order rate constant k_{meas} by accounting for the Pd metal catalyst content, showed an unambiguous volcano-shape dependence on Pd content (Fig. 6c).

For the most active catalyst (12.7 wt% Pd), the TCE conversion reached >99% in slightly over 1 h, with the products being mostly ethane (88%) plus a small, identifiable amount of ethene (0.2%). Interestingly, C_4 compounds were detected in increasing amounts with reaction time (Fig. 6d). Although the level of chlorination could not be determined, these butane/butene products were strong evidence of a coupling reaction progressing in parallel with the HDC reaction. These C_4 products were also found with pure Pd NPs, indicating that the coupling reaction was not unique to the Pd–Au combination. Lowry and Reinhard reported the presence of C_4 products during TCE HDC using Pd/Al_2O_3 [26]. Accounting for the coupling products, the carbon mass balance was in excess of 90%, which was typical for all catalyst compositions. The product distribution was also typical for the other catalyst compositions (Fig. 6d). We found that these NPs were also highly active for the HDC of dichloroethene isomers and perchloroethene [74].

The most active materials (12.7–17.9 wt% Pd) were found to have rate constants exceeding 1800 $L/g_{Pd}/min$ (Fig. 6c, Table 2). These compositions were significantly more active than unsupported 4-nm Pd-only NPs and Pd/Al_2O_3 (55 and 47 $L/g_{Pd}/min$), which can be attributed to the much higher Pd dispersion of the Pd/Au NPs. These were roughly twice as active than the most active 20-nm Pd/Au NP catalyst (943 $L/g_{Pd}/min$ [27]). This comparison is somewhat misleading, though, since the surface coverages are different (60–90% versus 33%, respectively). The 4-nm Pd/Au NPs with the closest surface coverage values (~24 and ~36%) have reaction rates of 819 and 1345 $L/g_{Pd}/min$, respectively, which are comparable to that of the 20-nm Pd/Au NPs.

3.3. Mass transfer analysis of NP-catalyzed TCEHDC

Because of the large magnitudes of the reaction rate constants, it was possible that mass transfer limitations were present during catalysis, leading to measured rate constants that underestimated intrinsic surface reaction rates. Two possible sources of mass transfer limitations were identified (Scheme 1): the diffusion through a boundary layer surrounding the catalytic NPs (mass transfer from bulk liquid to solid surface), and the transport across the headspace–water interface (mass transfer from bulk gas to bulk liquid).

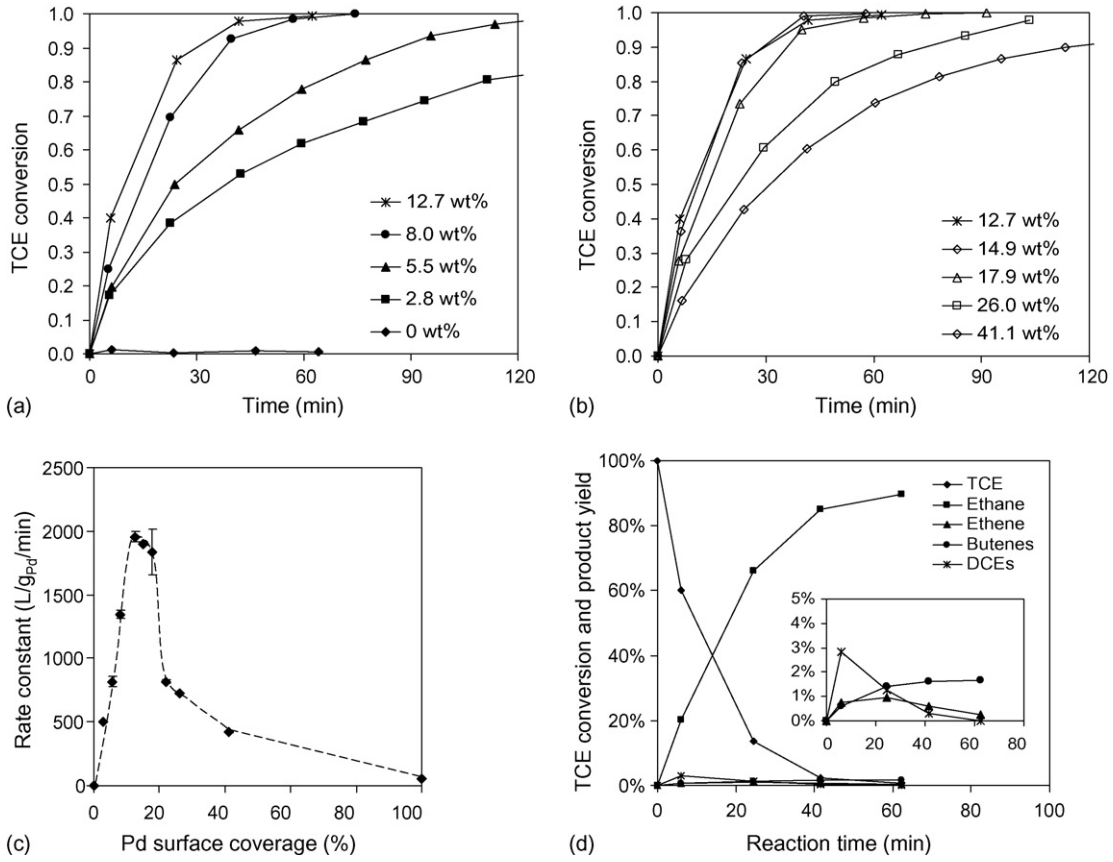

Fig. 6. TCE conversion-time profiles for Pd/Au NPs, with Pd loadings (a) 12.7 wt% and below, (b) 12.7 wt% and above, (c) Reaction rate constants plotted against Pd loadings, with dotted line drawn to guide the eye. Repeatability of catalyst runs was checked for several Pd/Au compositions (as indicated by error bars), and (d) TCE conversion and product distribution as functions of reaction time for Pd/Au NPs (12.7 wt% Pd).

The liquid-to-solid mass transfer step was considered first. At any given reaction time, the TCE molar flux to the NP catalyst surface is $W_{TCE} = k_{ls}C_{TCE,liq}$, where the effective liquid-to-catalytic-surface mass transfer coefficient $k_{ls} = k_r k_c/(k_r + k_c)$, k_c is the mass transfer coefficient, k_r is the surface reaction rate constant, and $C_{TCE,liq}$ is the TCE concentration in the bulk fluid. The molar flux W_{TCE} can be calculated from the rate of change in TCE concentration ($-dC_{TCE}/dt$) divided by the total surface area of all the NPs in the reaction volume (termed volumetric surface area, or VSA). This leads to $k_{ls}C_{TCE} = (k_{meas}C_{TCE})/VSA$, or $k_{ls} = k_{meas}/VSA$. For the most active Pd/Au NP catalyst (12.7 wt%), $k_{meas} = 1.43 \times 10^{-3}$ s^{-1} and VSA $= 2.09 \times 10^{-2}$ m^2 L^{-1} $= 2.09 \times 10^{-1}$ cm^{-1}, leading to $k_{ls} = 6.6 \times 10^{-3}$ cm s^{-1}.

The mass transfer coefficient k_c for TCE diffusing towards a spherical particle was calculated using the Frossling correlation, from which the Sherwood number Sh equals 2 in the limit of pure diffusion [75]. Since $Sh = k_c D_p/D_{TCE}$, where D_p is particle diameter and D_{TCE} is the diffusivity of TCE in water (1.04×10^{-5} cm^2 s^{-1} at 25 °C [46]), k_c was calculated to be

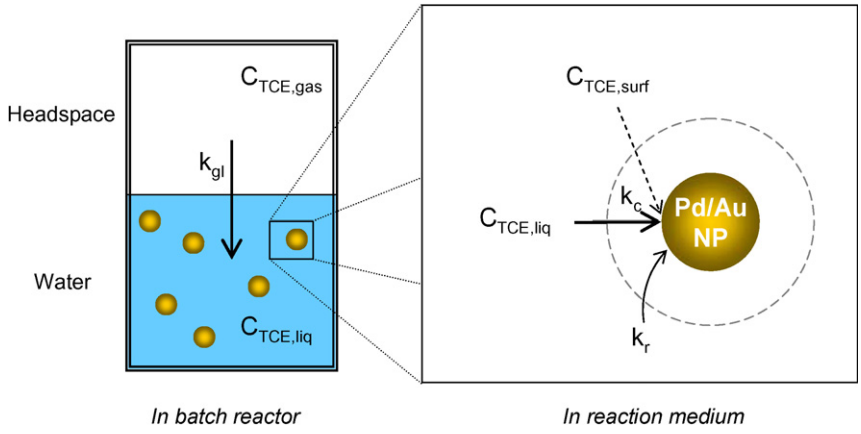

Scheme 1. Illustration of the possible mass-transfer bottlenecks in the TCE HDC reaction studies using Pd/Au NP catalysts.

52 cm s^{-1} for a particle diameter of 4 nm. Calculated to be 1.14×10^{-2} cm s^{-1} using the values of k_{ls} and k_c, the surface reaction rate k_r was much smaller in magnitude than k_c. For the most active catalyst then, it was concluded that TCE diffusion to the NP surface had a negligible effect on measured reaction rates.

The gas-to-liquid mass transfer step was considered next. At any given reaction time, W_{TCE} also equals the TCE molar flux from the headspace to the water phase, or $W_{TCE} = k_{gl}((K/RT) \times C_{TCE,liq} - C_{TCE,gas})$, where k_{gl} is the gas–liquid mass transfer coefficient, K is Henry's law constant (8.8×10^{-3} atm m^3 mol^{-1} for TCE in water at 25 °C), R is the ideal gas constant, and T is temperature. Using published mass transfer data on TCE aqueous solutions [76], k_{gl} was estimated to be 3.42×10^{-2} cm s^{-1}. This value was larger than k_{eff} but not overwhelmingly so, indicating that the effect of liquid–gas TCE mass transfer could not be neglected. The measured rate constants were thus corrected using the relation $k_{corr} = k_r \times VSA$, where $1/k_r = VSA/k_{meas} - 1/k_{gl}$ and $k_{meas} = k_{cat} \times C_{cat}$ (see supplemental information for derivation) (Table 2). The gas–liquid mass transfer effect roughly amounted to a 10% error in measured rates for the more active catalysts.

3.4. Possible explanations for volcano-shape HDC-coverage dependence.

Initial turnover frequencies (TOF's) for the Pd/Au NPs were calculated using $k_{cat,corr}$ (k_{corr}/C_{cat}) and initial TCE concentrations, and plotted against Pd content and Pd surface coverage (Table 2; Fig. 7a). Except for the inactive Au NPs, all NP samples had higher TOF's than pure Pd NPs (0.044 s^{-1}). The most active compositions were Au NPs with an incomplete shell of Pd atoms (i.e., decorated core bimetallic structure, as opposed to core/complete-shell bimetallic structure). Three activity regions could be observed: (I) in the 0–70% surface coverage range, TOF values increased from zero to a maximum of 1.47 s^{-1}; (II) in the 70–110% range, TOF values decreased to 0.57 s^{-1}; (III) above 110%, they decreased but to a lesser degree. The relationship

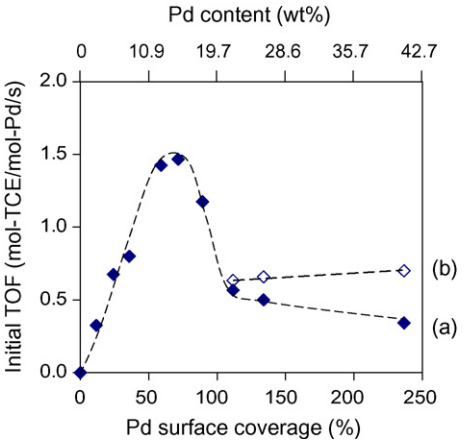

Fig. 7. (a) Initial TOF values normalized to total Pd content and plotted against Pd content and Pd surface coverage and (b) initial TOF values for Pd surface coverages of >100%, normalized to exposed Pd atom content.

between the measured TOF values and the elementary steps that comprise the TCE HDC reaction pathway (e.g., TCE adsorption, H_2 dissociative adsorption, TCE dechlorination, double-bond hydrogenation, and ethane desorption) is not known. The rate-limiting step could be C–Cl bond breaking, drawing on Zhou et al.'s surface science study of Pd-catalyzed dechlorination of fluorochloroethanes in which they reported that "the rate constant for the dechlorination step is an important contributor to the overall rate law for catalytic hydrodechlorination" [77]. It is known that chloroethenes adsorb at room temperature to form surface-bound hydrocarbon fragments and Cl atoms on Pd [78] and Pd–Cu alloy surfaces [79,80].

If isolated Pd atoms were the active sites, then TOF values should be constant with increasing Pd surface coverage in region I. The observed TOF increase indicates that individual Pd atoms are not the active sites, and suggests that two-dimensional ensembles or islands of Pd atoms are instead the active sites. Representative of a geometric effect, the activity increase could be functions of size and number of Pd ensembles. Lambert and co-workers showed through scanning tunneling microscopy that Pd atoms formed 1-atom-thick, 3-nm-wide ensembles on Au surface defects at low Pd surface coverages (specifically 7%) after annealing at 300 K [31]. Such nanosized Pd ensembles may be present in the Pd/Au NPs, in which they form on the Au NP surface defects during the room-temperature Pd salt reduction step. These proposed Pd ensembles would adsorb and activate both TCE [78] and H_2 for surface reaction.

Additionally, the Au surface is not known to adsorb either TCE or H_2, but the Pd–Au interface could adsorb TCE. We suggest that the interface between Pd and Au atoms provides another set of active sites for TCE HDC, like the Pd–Cu sites proposed by Barbosa, Jugnet, and co-workers for TCE adsorption [79,80]. Through surface science and density functional theory studies, they showed that TCE can adsorb at room temperature on two Pd and two Cu atoms to form two Pd–C bonds and two Cu–Cl bonds. Since chloride atoms can bind to Au surfaces [81], it is reasonable that TCE adsorbs similarly on mixed Pd–Au metal sites. Thus, an increasing number of Pd–Au sites could account for the TOF increase with Pd surface coverage.

We propose that the TOF decrease in region II is due to the formation of a second layer of Pd atoms before the completion of the first one, such that three-dimensional Pd ensembles are formed. This would lead to a decrease in Pd dispersion, in that not all the Pd atoms are accessible for TCE HDC. Indeed, Lambert and co-workers showed that a Au film with 70% Pd coverage contained three-dimensional Pd ensembles [31]. Gas-phase chemisorption measurements using H_2 or CO would be highly useful in quantifying Pd dispersion, but the colloidal state of the Pd/Au NPs presents challenges for this analytical technique. Another possible explanation is the reduction in the population of mixed Pd–Au metal sites with increasing Pd surface coverage.

In region III, the TOF decreases at a different rate with increasing Pd coverage. Above 100% Pd surface coverage, there are presumably no exposed Au atoms and therefore no mixed Pd–Au sites. Thus, the observed activity would be that of

exposed Pd atoms only. We re-calculated the TOF values in this region by using surface Pd atoms instead of total Pd atoms (Table 2, Fig. 7b). With the expectation that the TOF would be constant above 100% Pd coverage, we found the Pd/Au NPs to have comparable TOF values (in the range of ~0.6–0.7 s^{-1}). The upward trend in the re-calculated TOF's could be real or an artifact of the magic cluster approximation. These values are several times higher than the recalculated TOF for pure Pd NPs (0.13 s^{-1}), suggesting that the Pd catalytic activity was modified electronically by the underlying Au.

This possibility of catalytic promotion by an electronic effect is corroborated by the XPS results. We interpret the observed negative binding energy shifts of Pd 3d photoemission peaks with decreasing Pd surface coverage (Fig. 5) as the Pd metal gaining d-electron density as it covers progressively less Au NP surface [82]. Studies of other Pd–Au systems indicate either negligible [31,36,72,83] or significant electronic effects [32,70], which may be due to differences in sample preparation.

Gold is more expensive than palladium, but the Pd–Au combination is a more active catalyst than pure Pd. In terms of metals cost, we compared the most active NP composition (14.9 wt%) with pure Pd NPs of the same size. Using the spot prices for Au and Pd at the end of 2005 ($513/oz and $258/oz, respectively) and taking into account the reaction rates, we calculated that the Pd/Au NPs were 2.9 times more cost-effective as a catalyst than the Pd NPs.

3.5. Immobilizing Pd/Au NPs on a support.

Electrostatic adsorption was used to immobilize the Pd/Au NPs on a porous solid support. In this method, a metal oxide develops a surface charge based on the fluid pH and its isoelectric point (iep). The iep values for Al_2O_3, MgO, and SiO_2 are 5–6, 12, and 2, respectively [84]. At pH values above the iep (at which the net surface charge is zero), the support surface is negatively charged; at pH values below the iep, the surface is positively charged. The Pd/Au NPs (and Au NPs) are negatively charged according to electrophoretic mobility measurements, and so positively charged supports would be needed.

To demonstrate that charge interactions can be used for immobilization, we contacted Au NP sols with Al_2O_3 (at two different pH values, 3 and 6), MgO (at pH 6), and SiO_2 (at pH 6), and measured the amount of initial uptake (Fig. 8). At pH 6, Al_2O_3 and SiO_2 showed little adsorption for the NPs, since the pH was close to their IEP values. Reducing the pH to 3 using HCl, Al_2O_3 showed a significant increase in NP adsorption, consistent with the surface being more positively charged. The basic MgO support also showed significant NP adsorption at pH 6, as expected.

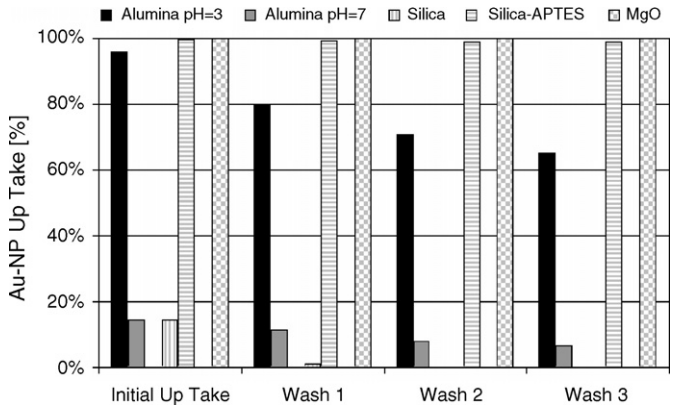

Fig. 8. Extent of Au NP adsorption (initial uptake) and release after several washes for the various supports.

Table 3
Supported Pd/Au NP catalyst compositions and rate constants

Support	Pd loading of total catalyst (wt%)	Au loading of total supported (wt%)	First-order rate constant k_{cat} (L/g_{Pd}/min)
Unsupported[a]	–	–	1956
MgO[a]	0.014	0.10	1670
Amine-containing SiO_2[a]	0.040	0.23	983
Control: Pd/Al_2O_3	1	0	47

[a] Pd content of Pd/Au NPs = 12.7 wt%.

The stability of the immobilized NPs was tested for each support by rinsing the resultant powders with water (pH 6) several times. The loss of NPs was most apparent for the Al_2O_3-supported NPs immobilized at pH 3, in which the pH of the wash was insufficient to maintain the Al_2O_3 surface charge. On the other hand, no NPs were removed from the MgO since the surface remained positively charged during the washes. Functionalizing the SiO_2 with amine surface groups significantly increased the adsorption and retention of NPs (Fig. 8). The amine groups were protonated and positively charged at pH values below 10, thereby generating the desired positive surface charge.

Using functionalized SiO_2 and MgO, we immobilized Pd/Au NPs (12.7 wt% Pd) and tested the resultant supported catalysts for TCE HDC. Both materials were very active for the reaction, but less active than the unsupported Pd/Au NPs. Possible explanations for the reduced reaction rates are intraparticle mass transfer within the porous support and the loss of a portion of the Pd/Au NP surface due to contact with the oxide surface. In spite of these issues, the resulting supported Pd/Au NP catalysts were still significantly more active than the commercial source of Pd/Al_2O_3 (Table 3).

4. Conclusions

Pd/Au bimetallic NPs with a 4-nm Au core and controlled Pd loading were synthesized successfully, with all compositions more active for the aqueous-phase TCE HDC reaction than Pd-only catalysts. This material exhibited a well-defined volcano-shape activity dependence on Pd loading. Analysis of the batch reaction indicated that the liquid-to-particle surface mass transfer effect was negligible but the gas-to-liquid mass transfer effect was not. The TOF values (as moles of TCE converted per mole of Pd atoms per second) were corrected for the latter, and correlated to Pd surface coverage. Surface coverage was determined by modeling Pd/Au NPs as magic clusters with seven shells of Au atoms and the Pd atoms in the 8th shell. The reaction data suggested geometric effects were responsible for enhanced TCE HDC activity (i.e., that Pd ensembles and Pd–Au mixed sites can

participate as adsorption and surface reaction sites). The binding energy shifts of Pd metal with surface coverage suggested the possibility of catalyst promotion by an electronic effect. The very active compositions had a decorated core bimetallic nanostructure, exhibiting TOF's on the order of $1\ s^{-1}$. Stable immobilization of the NPs was accomplished by electrostatically binding them to the positively charged surfaces of MgO and amine-functionalized SiO_2. These supported Pd/Au NPs will serve as a model material for continuous-flow reaction and chemisorption studies. X-ray absorption spectroscopic studies to confirm the Pd-on-Au bimetallic distribution of the NPs are currently underway.

5. Supplemental Information

For the general case in which mass transfer limitations due to gas–liquid transport and liquid-to-surface transport occur in series with the reaction on the particle surface under pseudo-steady-state conditions, it can be readily shown that the overall mass transfer coefficient $k_{overall}$ is given as $1/k_{overall} = 1/k_{gl} + 1/k_{ls} = 1/k_{gl} + 1/k_c + 1/k_r$, where the TCE molar flux $W_{TCE} = k_{overall} \times C_{TCE}$. Since W_{TCE} is equal to $(-dC_{TCE}/dt)/VSA$, this relation leads to $k_{overall} = k_{meas}/VSA$ or $k_{meas} = k_{overall} \times VSA$. So it follows that the corrected rate constant is $k_{corr} = k_r \times VSA$, where $1/k_r = 1/k_{overall} - 1/k_{gl} - 1/k_c$. It was already shown that $k_c \gg k_r$, so therefore $1/k_r = 1/k_{overall} - 1/k_{gl}$, or $1/k_r = VSA/k_{meas} - 1/k_{gl}$.

Acknowledgements

We thank Mr. W.V. Knowles for collecting the TEM images, Ms. J. Yu for assistance with silica modification with APTES, Ms. A. Takemura for assistance with experiments, Mr. S. Khapli for assistance with the XPS data collection, Mr. V.S. Murthy for assistance with the illustrations, Prof. J.W. Hightower for helpful discussions, and Mr. E. Munoz for assistance on the magic cluster equations. We gratefully acknowledge the financial support of the National Science Foundation (EEC-0118007) and SABIC Americas.

References

[1] P.J. Squillace, M.J. Moran, W.W. Lapham, C.V. Price, R.M. Clawges, J.S. Zogorski, Environ. Sci. Technol. 33 (1999) 4176–4187.
[2] H.H. Russell, J.E. Matthews, G.W. Sewell, TCE Removal from Contaminated Soil and Ground Water, EPA (US Environmental Protection Agency), 1992.
[3] C. Collins, F. Laturnus, A. Nepovim, Environ. Sci. Pollut. Res. 9 (2002) 86–94.
[4] ATSDR, CERCLA Priority List of Hazardous Substances, Agency for Toxic Substances and Disease Registry-US Department of Health and Human Services, 2003.
[5] E.C. Butler, K.F. Hayes, Environ. Sci. Technol. 33 (1999) 2021–2027.
[6] ATSDR, Agency for Toxic Substances and Disease Registry-US Department of Health and Human Services, 2003.
[7] ATSDR, Toxicological Profile for Trichloroethylene, Agency for Toxic Substances and Disease Registry-US Department of Health and Human Services, 1997.
[8] EPA, Technical Protocol for Evaluating Natural Attenuation of Chlorinated Solvents in Ground Water, EPA (US Environmental Protection Agency), 1998.
[9] C.S. Carr, S. Garg, J.B. Hughes, Environ. Sci. Technol. 34 (2000) 1088–1094.
[10] M. Lowe, E.L. Madsen, K. Schindler, C. Smith, S. Emrich, F. Robb, R.U. Halden, FEMS Microbiol. Ecol. 40 (2002) 123–134.
[11] EPA, In situ thermal treatment of chlorinated solvents: Fundamentals and Field Applications, EPA (US Environmental Protection Agency), 2004.
[12] W.X. Zhang, C.B. Wang, H.L. Lien, Catal. Today 40 (1998) 387–395.
[13] W. Zhang, J. Nanopart. Res. 5 (2003) 323–332.
[14] F. Alonso, I.P. Beletskaya, M. Yus, Chem. Rev. 102 (2002) 4009–4092.
[15] F.J. Urbano, J.M. Marinas, J. Mol. Catal. A Chem. 173 (2001) 329–345.
[16] R. Muftikian, Q. Fernando, N. Korte, Water Res. 29 (1995) 2434–2439.
[17] H.L. Lien, W.X. Zhang, Colloid Surf. A Physicochem. Eng. Asp. 191 (2001) 97–105.
[18] H.L. Lien, W.X. Zhang, J. Environ. Eng. ASCE 125 (1999) 1042–1047.
[19] C.B. Wang, W.X. Zhang, Environ. Sci. Technol. 31 (1997) 2154–2156.
[20] C.G. Schreier, M. Reinhard, Chemosphere 31 (1995) 3475–3487.
[21] W.W. McNab, R. Ruiz, Chemosphere 37 (1998) 925–936.
[22] C. Schuth, M. Reinhard, Appl. Catal. B Environ. 18 (1998) 215–221.
[23] G.V. Lowry, M. Reinhard, Environ. Sci. Technol. 33 (1999) 1905–1910.
[24] G.V. Lowry, M. Reinhard, Environ. Sci. Technol. 34 (2000) 3217–3223.
[25] C. Schuth, S. Disser, F. Schuth, M. Reinhard, Appl. Catal. B Environ. 28 (2000) 147–152.
[26] G.V. Lowry, M. Reinhard, Environ. Sci. Technol. 35 (2001) 696–702.
[27] M.O. Nutt, J.B. Hughes, M.S. Wong, Environ. Sci. Technol. 39 (2005) 1346–1353.
[28] V.N.M. Rao, Hydrodehalogenation Catalysts and their Preparation and Use, US Patent 5,447,896, 1995.
[29] M. Bonarowska, A. Malinowski, W. Juszczyk, Z. Karpinski, Appl. Catal. B Environ. 30 (2001) 187–193.
[30] M. Bonarowska, B. Burda, W. Juszczyk, J. Pielaszek, Z. Kowalczyk, Z. Karpinski, Appl. Catal. B Environ. 35 (2001) 13–20.
[31] C. Baddeley, R. Ormerod, A. Stephenson, R. Lambert, J. Phys. Chem. 99 (1995) 5146–5151.
[32] D.I. Enache, J.K. Edwards, P. Landon, B. Solsona-Espriu, A.F. Carley, A.A. Herzing, M. Watanabe, C.J. Kiely, D.W. Knight, G.J. Hutchings, Science 311 (2006) 362–365.
[33] L. Guczi, A. Beck, A. Horvath, Z. Koppany, G. Stefler, K. Frey, I. Sajo, O. Geszti, D. Bazin, J. Lynch, J. Mol. Catal. A Chem. 204 (2003) 545–552.
[34] A.M. Venezia, V. La Parola, G. Deganello, B. Pawelec, J.L.G. Fierro, J. Catal. 215 (2003) 317–325.
[35] M. Neurock, W.D. Provine, D.A. Dixon, G.W. Coulston, J.J. Lerou, R.A. van Santen, Chem. Eng. Sci. 51 (1996) 1691–1699.
[36] M. Chen, D. Kumar, C. Yi, D.W. Goodman, Science 310 (2005) 291–293.
[37] W.D. Provine, P.L. Mills, J.J. Lerou, Stud. Surf. Sci. Catal. 101 (1996) 191.
[38] M. Nakamura, Y. Fujiwara, T. Yasui, Method of producing vinyl acetate, US Patent #4,087,622, 1978.
[39] T.C. Bissot, Surface Impregnated Catalysts, US Patent #4,048,096, 1977.
[40] V. Ponec, G.C. Bond, Catalysis by Metals and Alloys, Elsevier, 1995.
[41] M. Boudart, H.S. Hwang, J. Catal. 39 (1975) 44.
[42] B. Coq, F. Figueras, J. Mol. Catal. A Chem. 173 (2001) 117–134.
[43] J.W. Slot, H.J. Geuze, Eur. J. Cell Biol. 38 (1985) 87–93.
[44] ImageJ, 1.34s, 2005 http://rsb.info.nih.gov/ij/.
[45] NIST X-ray Photoelectron Spectroscopy Database, Version 3.4, 2005 http://srdata.nist.gov/xps/Elmcomp.asp.
[46] R.P. Schwarzenbach, P.M. Gschwend, D.M. Imboden, Environmental Organic Chemistry, John Wiley & Sons, Inc., New York, 1993.
[47] M.C. Daniel, D. Astruc, Chem. Rev. 104 (2004) 293–346.
[48] L.D. Rampino, K.E. Kavanagh, F.F. Nord, Proc. Natl. Acad. Sci. U.S.A. 29 (1943) 246–256.
[49] N. Toshima, T. Takahashi, Bull. Chem. Soc. Jpn. 65 (1992) 400–409.
[50] M.A. Watzky, R.G. Finke, J. Am. Chem. Soc. 119 (1997) 10382–10400.
[51] S.Y. Troitski, M.A. Serebriakova, M.A. Fedotov, S.V. Ignashin, A.L. Chuvilin, E.M. Moroz, B.N. Novgorodov, D.I. Kochubey, V.A.

Likholobov, B. Blanc, P. Gallezot, J. Mol. Catal. A Chem. 158 (2000) 461–465.
[52] D. Kashchiev, G.M. van Rosmalen, Cryst. Res. Technol. 38 (2003) 555–574.
[53] K.I. Popov, S.S. Djokic, B.N. Grgur, Fundamental Aspects of Electrometallurgy, Kluwer Academic/Plenum Publishers, New York, 2002.
[54] A.F. Lee, C.J. Baddeley, C. Hardacre, R.M. Ormerod, R.M. Lambert, G. Schmid, H. West, J. Phys. Chem. 99 (1995) 6096–6102.
[55] G. Schmid, H. West, H. Mehles, A. Lehnert, Inorg. Chem. 36 (1997) 891–895.
[56] K.R. Brown, M.J. Natan, Langmuir 14 (1998) 726–728.
[57] N.R. Jana, L. Gearheart, C.J. Murphy, Adv. Mater. 13 (2001) 1389–1393.
[58] B. Nikoobakht, M.A. El-Sayed, Chem. Mater. 15 (2003) 1957–1962.
[59] J.H. Song, F. Kim, D. Kim, P.D. Yang, Chem. Eur. J. 11 (2005) 910–916.
[60] S. Asokan, K.M. Krueger, A. Alkhawaldeh, A.R. Carreon, Z. Mu, V.L. Colvin, N. Mantzaris, M.S. Wong, 16, (2005) 2000–2011.
[61] I. Mekis, D.V. Talapin, A. Kornowski, M. Haase, H. Weller, J. Phys. Chem. B 107 (2003) 7454–7462.
[62] X. Peng, M.C. Schlamp, A.V. Kadavanich, A.P. Alivisatos, J. Am. Chem. Soc. 119 (1997) 7019–7029.
[63] M. Okada, S. Ogura, W.A. Dino, M. Wilde, K. Fukutani, T. Kasai, Appl. Catal. A Gen. 291 (2005) 55–61.
[64] A.C. Gluhoi, H.S. Vreeburg, J.W. Bakker, B.E. Nieuwenhuys, Appl. Catal. A Gen. 291 (2005) 145–150.
[65] P. Claus, Appl. Catal. A Gen. 291 (2005) 222–229.
[66] L. Lewis, Chem. Rev. 93 (1993) 2692–2730.
[67] J. Thomas, Pure Appl. Chem 60 (1988) 1517–1528.
[68] T. Teranishi, M. Miyake, Chem. Mater. 10 (1998) 594–600.
[69] J.C. Slater, J. Chem. Phys. 41 (1964) 3199.
[70] P.A.P. Nascente, S.G.C. Decastro, R. Landers, G.G. Kleiman, Phys. Rev. B 43 (1991) 4659–4666.
[71] A.M. Venezia, L.F. Liotta, G. Pantaleo, V. La Parola, G. Deganello, A. Beck, Z. Koppany, K. Frey, D. Horvath, L. Guczi, Appl. Catal. A Gen. 251 (2003) 359–368.
[72] V.I. Parvulescu, V. Parvulescu, U. Endruschat, G. Filoti, F.E. Wagner, C. Kubel, R. Richards, Chem. Eur. J. 12 (2006) 2343–2357.
[73] R.J. Farrauto, J.K. Lampert, M.C. Hobson, E.M. Waterman, Appl. Catal. B Environ. 6 (1995) 263–270.
[74] K.N. Heck, M.O. Nutt, M.S. Wong, unpublished results, 2006.
[75] P. Harriott, AIChE 8 (1962) 93–101.
[76] P. Roberts, P. Dandllker, Environ. Sci. Technol. 17 (1983) 484–489.
[77] G. Zhou, C. Chan, A.J. Gellman, J. Phys. Chem. B. 103 (1999) 1134–1143.
[78] K.T. Park, K. Klier, C.B. Wang, W.X. Zhang, J. Phys. Chem. B 101 (1997) 5420–5428.
[79] Y. Jugnet, J.C. Bertolini, L.A.M.M. Barbosa, P. Sautet, Surf. Sci. 505 (2002) 153–162.
[80] L.A.M.M. Barbosa, P. Sautet, J. Catal. 207 (2002) 127–138.
[81] G.N. Kastanas, B.E. Koel, Appl. Surf. Sci. 64 (1993) 235–249.
[82] D.R. Rainer, J.S. Corneille, D.W. Goodman, J. Vac. Sci. Technol. A 13 (1995) 1595–1599.
[83] B.E. Koel, A. Sellidj, M.T. Paffett, Phys. Rev. B 46 (1992) 7846–7856.
[84] G.A. Parks, Chem. Rev. 65 (1965) 177–198.